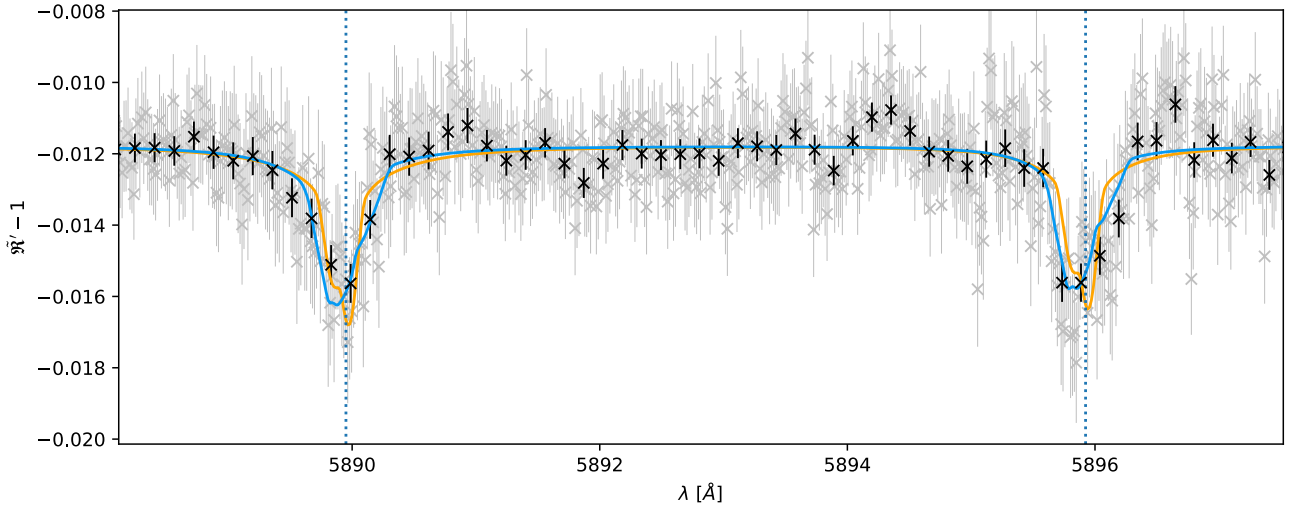

Fig. 5. Best fit of isothermal line retrieval with an added day- to nightside wind in the lower atmosphere without a $\cos\theta$ dependence and a vertical wind in the upper atmosphere in blue on the dataset in grey. The day- to nightside wind without a $\cos\theta$ dependence throughout the atmosphere (moderate evidence) is shown for comparison purposes in orange. According to the Jeffrey scale, which is logarithmic, the best-fit model in blue has a probability higher than an order of magnitude than the moderate evidence model in orange. The data were binned by ten bins in black for better visualisation. The sodium doublet line centres are indicated by dashed vertical blue lines.

super-rotational wind. While this would be an excellent fit for a very broad but shallow sodium doublet, it does not work similarly for the deep sodium lines in this dataset. To subsequently offset the lack of unshifted parts of the atmosphere that would sit at the centre, the retrieval increases the temperature, which is the main driver of the line depth. This leads to retrieved temperatures well beyond 4000 K, which are not physically sensible for an ultra-hot Jupiter with the system parameters of WASP-76 b (see Table 1 and the posterior distributions in Appendix A) and are ruled out via the prior. Additional evidence for this line of thought comes from the combined two-layer models, in which part of the atmosphere has the sodium lines unshifted, but broadened by vertical wind, and part of the atmosphere is dominated by either a day- to nightside or a super-rotational wind. In this scenario, the day- to nightside wind is preferred over the super-rotational wind, as predicted ($|\ln \mathcal{B}_{01}| = 2.31$, moderate evidence within the uncertainty). With ESPRESSO, the resolution would be sufficient to show this split into two peaks of the sodium line, provided that the S/N is sufficient and that super-rotation is the dominant wind pattern in the atmosphere and not super-imposed with other wind patterns that leave parts of the atmosphere at net zero wind speed (e.g. a combination with day- to nightside winds).

4.4. Two-layer patterns

To approximate a more realistic structure of exoplanet atmospheres, we divided the atmosphere into a lower and higher atmosphere and allowed for different wind patterns in the two layers. In the lower layer, we applied a day- to nightside or a super-rotational wind, and a vertical wind in the higher layer. The first question was where to set the boundary between the two layers. As shown by Seidel et al. (2020b), the additional parameter for the switch of layers introduces too many variables so that proper convergence of the retrieval is not possible. Because of the log-scale of the pressure, which serves as a proxy for relative height above the surface, only a few values for the layer switch are sensible and a restriction beyond an order of magnitude estimate is not necessary, especially because there will most likely be a transition zone between the wind patterns. Assuming a surface pressure at the continuum of 10 bar, as is customary in the literature (e.g. Lecavelier Des Etangs et al. 2008; Agúndez et al. 2014; Line et al. 2014; Pino et al. 2018), we explored layer switches at 10^{-3} bar, 10^{-4} bar, and 10^{-5} bar. 10^{-3} bar compared to the continuum pressure because the lowest value corresponds to the location of the jets found for hot Jupiters in GCM modelling (Showman et al. 2009). We therefore know a priori that zonal winds dominate the atmosphere below this threshold. As is evident from the posterior plots for a layer switch at 10^{-5} bar (see Figs. A.7 and A.10), this switch is set too high and cannot properly constrain the upper layer. The preferred switch of layers, if any, should therefore lie between these two values. A switch between dynamical regimes at 10^{-3} bar, as predicted by GCM results, is preferred with at least $|\ln \mathcal{B}_{01}| = 4.56$ (strong evidence within the uncertainty of the results) independently of the assumed dynamics in the lower layer (dtn, srot, or ver). We thus fixed the pressure switch at 10^{-3} bar for the two-layer pattern models.

Of these models, a uniform day- to nightside wind has the highest evidence in the lower atmosphere, with moderate evidence over the super-rotational wind and weak evidence over a $\cos\theta$ latitude dependence of the wind, which are the next-best two models. Therefore the model with a vertical wind in the upper and day- to nightside wind in the lower atmosphere is preferred over any other model. The preference for a uniform wind in the lower atmosphere over the $\cos\theta$ latitude dependence implies that if the winds in the lower atmosphere in WASP-76 b are restricted to a jet-like band at the equator, it has to be relatively broad, spanning at least farther in latitude than a scaling through solid-body rotation suggests (>30°). The higher evidence for a day- to nightside wind over a super-rotational wind stems from a visible offset of the sodium doublet to the blue, as highlighted in Tabernero et al. (2021), where a median offset of -5.4 ± 2.6 for all detected lines was found. The posterior distribution of the best-fit model is shown in Fig. 6, and the resulting retrieved transmission spectrum is overplotted on the data in

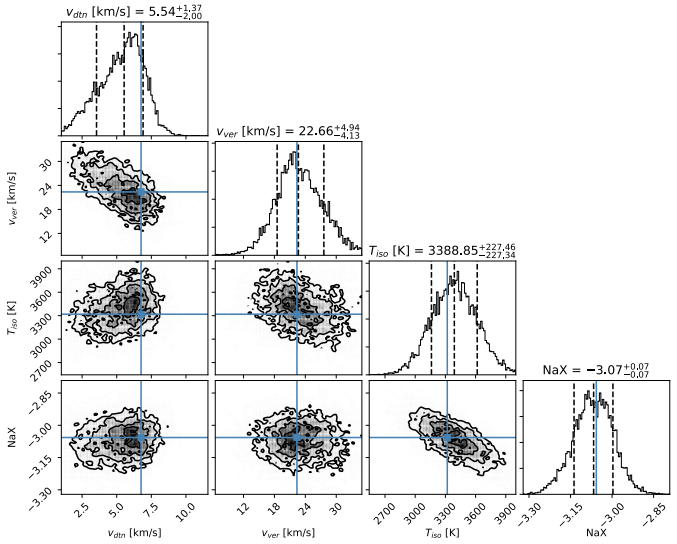

Fig. 6. Posterior distribution of isothermal line retrieval with an added day- to nightside wind in the lower atmosphere and a vertical wind in the upper atmosphere. The change of layers was set at $p = 10^{-3}$ bar, with the pressure at the surface set to $P_0 = 10$ bar.

Fig. 5. The day- to nightside wind has a speed of $5.5^{+1.4}_{-2.0}$ km s^{-1}, while the vertical wind shows speeds of $22.7^{+4.9}_{-4.1}$ km s^{-1}. Because we took planetary rotation into account under the assumption of tidal locking, these wind speeds are not upper limits, but constrain the possible wind speeds in the atmosphere of WASP-76 b to within 30% for the lower layer and 20% for the upper layer (see uncertainty of the retrieval). However, as discussed in Sect. 2.3, because of the necessary exposure time, the lines will be smeared by one resolution element in each direction, which increases the error on the wind speed for the radial outwards wind by roughly 10% (dominated by the width) and also by roughly 10% for the day- to nightside wind (lower absolute wind speed, but dominated by the line position). This has no effect on the overall conclusions on the wind patterns we present in the studied system.

5. Discussion

Recently, Ehrenreich et al. (2020) studied WASP-76 b using ESPRESSO through the atomic iron signature and found a significant asymmetry between the first and second half of the transit, leading to a one-sided shift of the signature. At first, the iron detection shows no shift during ingress and then moves to a constant blueshift of 11.0 ± 0.7 km s^{-1}. Taking planetary rotation into account, they concluded that the lower atmosphere of WASP-76 b shows a day- to nightside wind of 5.3 km s^{-1}. The result, a best-fit to the sodium doublet with a day- to nightside wind of $5.5^{+1.4}_{-2.0}$ km s^{-1}, is compatible with their findings in the lower atmosphere in which iron is present (at pressures higher than the micro bar level). This result is driven by the detected offset of the lines to the blue by $\sim$5 km s^{-1} in Tabernero et al. (2021), which is confirmed in this work and can either be induced by a day- to nightside wind over the entire planet or by a super-rotational wind with condensation of sodium on the nightside. Because the condensation temperature of sodium (50% condensated with $T \approx 1000$ K; Lodders 2003) is much too low for the nightside temperature of an ultra-hot Jupiter (Parmentier et al. 2018), we rule out an asymmetrical super-rotational wind. A similar offset observation was made for WASP-121 b, another ultra-hot Jupiter (Borsa et al. 2021). In the our analysis, we neglected the RM effect, which was taken into account by Ehrenreich et al. (2020). The verification of the wind pattern from Ehrenreich et al. (2020) thus additionally confirms the negligible RM effect for this particular system.

None of the studies analysing wind patterns in the lower atmosphere, however, are capable of probing what occurs in the intermediate atmosphere between the mass-loss in the exosphere and the various zonal wind patterns in the lower atmosphere. We show through atmospheric retrieval that these layers are connected by a strong vertical wind of $22.7^{+4.9}_{-4.1}$ km s^{-1} for WASP-76 b. Seidel et al. (2020b) observed a similar phenomenon for HD 189733 b that was later confirmed through independent observations by Keles et al. (2020). This vertical wind can either be an outward-expanding wind, where the material does not descend towards lower atmospheric layers, or the vertical parts of large cell-like structures, where the upper zonal arm of the cell is in the thermosphere. Assuming this large cell-like structure, the upper zonal arm would not affect the sodium-line shape because sodium would be ionised at these altitudes and only recombine in the downwards vertial arm of the cell. Because of the nature of transmission observations over the terminator, these two wind patterns cannot be distinguished. In the case of HD 189733 b, the interaction of ions in the lower atmosphere with the surprisingly strong estimated magnetic field (Cauley et al. 2019) could be a possible explanation of a purely expanding wind (Seidel et al. 2020b), dragging neutral sodium upwards. For WASP-76 b, no indirect magnetic field strength estimates are available, but if the same mechanism is at work for this exoplanet, the magnetic field strength should be comparable to the magnetic field strengths observed in the sample of Cauley et al. (2019), orders of magnitude higher than the magnetic field of Jupiter.

The observed vertical wind, regardless of its origin, feeds material up to the thermosphere, where it could be further heated and escape through hydrodynamic escape. This has not been directly observed for WASP-76 b, but strong planetary winds, bordering on hydrodynamical escape, are predicted for WASP-76 b (see Salz et al. 2016, Fig. 3, for $\log_{10} \Phi_G(\text{WASP} - 76\text{ b}) \approx 13$). This is compatible with the results by Seidel et al. (2019), who showed that sodium expands far above the surface, but velocities remain just below the escape velocity for WASP-76 b. The revised escape velocity with the updated planetary radius and mass is 41 ± 1 km s^{-1}, significantly higher than the vertical wind speeds retrieved for sodium. Therefore the vertical wind is a transport mechanism for material to the thermosphere, but not the direct driver of atmospheric escape. However, it is important to note that due to the integration over the entire atmosphere, variations in wind speed within the two atmospheric regimes are not accounted for, but rather, a mean wind velocity is derived. Whether the expanding wind gains momentum with height, driven by processes in the thermosphere, or fuels it itself is consequently unclear.

While the result provides compelling evidence for the case of strong vertical winds in the upper atmosphere, there are competing ideas to explain the broad line shape of sodium in hot Jupiters: for a low sodium abundance, the sodium might form an optically thin cloud high up in the atmosphere, producing a very broad feature. However, this is dependent on the line ratio and has been shown not to apply to WASP-76 b (Gebek & Oza 2020). Additionally, more complex temperature profiles might apply for WASP-76 b, varying in latitude or longitude, which the retrieval cannot account for. While the line shape is sensitive to

the temperature through thermal broadening, it cannot produce the line shape observed for the sodium doublet in hot Jupiters (Wyttenbach et al. 2015; Huang et al. 2017; Seidel et al. 2020b). Another caveat is the assumption of local thermodynamic equilibrium (LTE), which excludes any non-LTE effects that might affect the line shape. Recently, Fisher & Heng (2019) quantified this assumption and highlighted that currently, LTE and non-LTE atmospheres cannot be distinguished. This strengthens the case for strong vertical winds.

Zhang (2020) recently reviewed the current knowledge regarding temperature profiles for ultra-hot Jupiters (defined as having equilibrium temperatures higher than ~2200 K). Temperature inversions were confirmed through emission observations for KELT-9 b (Pino et al. 2020), WASP-121 b (Evans et al. 2017; Bourrier et al. 2020), a planet similar to WASP-76 b, for WASP-18 b (Sheppard et al. 2017), for WASP-189 b (Yan et al. 2020), and WASP-33 b (Haynes et al. 2015; Nugroho et al. 2017). Nonetheless, temperature inversions are not established as an unequivocal feature of ultra-hot Jupiters because some, for example, WASP-12 b and WASP-103 b, have spectra consistent with blackbody radiation, suggesting isothermal atmospheres (Arcangeli et al. 2018; Parmentier et al. 2018; Kreidberg et al. 2018). As a caveat, these observations stem from WFC3, and the black-body spectra in the covered band could also be explained with a temperature inversion, which might attribute these outliers to observational limitations. TiO and VO have been suggested as two possible drivers of thermal inversion by heating the upper atmosphere (Hubeny et al. 2003; Fortney et al. 2008), although discussions of the mechanisms of thermal inversions are still ongoing (Mollière et al. 2015; Lothringer & Barman 2019; Gandhi & Madhusudhan 2019), and atomic metals were suggested as an alternative inversion agent (e.g. ZrO) (Lothringer & Barman 2019; Tabernero et al. 2021). This additional caveat is especially important because some of the mentioned works on temperature inversions are disputed, for example in WASP-33 b, where the features seen in Nugroho et al. (2017) could not be confirmed by Herman et al. (2020), but were again seen tentatively in Serindag et al. (2021). Nugroho et al. (2020) even found iron lines in emission, strengthening the case for additional causes of inversion layers in addition to TiO and VO. Assuming TiO and VO as the main drivers of inversion layers, Tabernero et al. (2021) ruled out TiO and VO down to a level of <10 ppm, and in line with the reasoning from Nugroho et al. (2017), they suggested that TiO and VO might be hidden below stronger features or be very weak, with another possibility being that both are transported from the dayside to the nightside by a day- to nightside wind where they condense out of the atmosphere. While the retrieval presented here cannot and does not aim to shed light on the detailed temperature structure of WASP-76 b, an isothermal temperature profile does not disagree with the current knowledge about ultra-hot Jupiters. The suggestion of day- to nightside winds from Tabernero et al. (2021) to explain their findings on TiO and VO is consistent with our results for the winds.

As already mentioned in Sect. 4, the temperature retrieved here is surprisingly high when compared to the equilibrium temperature and would lead to the ionisation of sodium, which we estimated with FastChem (Stock et al. 2018). At the equilibrium temperature of the planet, sodium remains in its neutral state at a fairly constant abundance up to 10^{-5} bar, whereas at temperatures of 3300 K and beyond, sodium ionises far lower in the atmosphere, in disagreement with the detected and confirmed sodium feature. This apparent inconsistency, where the retrieved temperature implicates an improbably high initial sodium abundance to compensate for ionisation, merits a more detailed investigation. Instead of concluding that a non-physical initial sodium abundance has to be present in ultra-hot Jupiters, it is more likely that vertical winds, such as found here, which interact with the sodium in the atmosphere, inevitably alter the density profile of sodium, away from a hydrostatic description of the atmosphere. In practice, the modified density profile will inflate the line depth, which has to then be compensated for with a higher homogeneous sodium abundance in the hydrostatic model. In conclusion, while a change in density profile has no significant effect on the line shape and therefore our results, winds will modify density profiles. Studies hoping to fit sodium abundances in low or high resolution have to account for the density profile of sodium generated by mid-latitude winds such as detected in this work.

6. Conclusions

We have studied winds in the atmosphere of the ultra-hot Jupiter WASP-76 b through its resolved sodium doublet. The transmission spectrum in the wavelength range of the sodium doublet is composed of two nights of ESPRESSO data (Ehrenreich et al. 2020; Tabernero et al. 2021) and the reprocessed HARPS dataset published by Seidel et al. (2019), which were combined thorugh S/N weighing. We introduced an update to the MERC code from Seidel et al. (2020b), which now takes planetary rotation into account and allows latitude-dependent zonal wind patterns. We found no evidence that a temperature gradient is preferred over an isothermal atmosphere. We combined the isothermal temperature profile with a uniform day- to nightside wind, a latitude-dependent day- to nightside wind, a uniform super-rotational wind, a latitude-dependent super-rotational wind, a vertical wind, and a two-layer combination of either day- to nightside or super-rotational winds in the lower and the vertical wind in the upper atmosphere.

The best-fit model is a uniform day- to nightside wind in the lower atmosphere of $5.5^{+1.4}_{-2.0}\,\mathrm{km\,s^{-1}}$ with a vertical, most likely mainly expanding wind in the upper atmosphere of $22.6^{+4.9}_{-4.1}\,\mathrm{km\,s^{-1}}$. Assuming a surface pressure of $P_0 = 10$ bar, the switch between the two layers is set at $p = 10^{-3}$ bar. For all models, we retrieved an isothermal temperature between 3300−3400 K and discussed that this overestimate is most likely a direct result of the effect of winds on the density profile of sodium in WASP-76 b. This is an important caveat for future studies regarding the fit of abundances from spectral lines. Our findings are compatible with the current literature on the wind dynamics of lower atmospheres and temperature profiles of hot and ultra-hot Jupiters, especially with previous work on WASP-76 b. Ehrenreich et al. (2020) used the time-resolved iron detection with ESPRESSO and reported a day- to nightside wind of $5.3\,\mathrm{km\,s^{-1}}$. This result is corroborated by our findings in this study. Additionally, we demonstrated a need for vertical winds in the intermediate atmosphere of these highly irradiated gas giants through their broadened features.

Our work proves the effectiveness of direct retrieval on resolved spectral lines to constrain possible wind patterns as input for more in-depth theoretical studies and the crucial role of high-resolution spectrographs for atmospheric characterisation. Our findings show a clear need for more detailed climate simulations that take the higher layers of the atmosphere into account to draw a clear picture of the atmospheres of ultra-hot exoplanets.

Acknowledgements. This project has received funding from the European Research Council (ERC) under the European Union's Horizon 2020 research and innovation programme (project FOUR ACES; grant agreement No. 724427).

This work has been carried out within the frame of the National Centre for Competence in Research 'PlanetS' supported by the Swiss National Science Foundation (SNSF). This work was supported by FCT – Fundação para a Ciência e Tecnologia (FCT) through national funds and by FEDER through COMPETE2020 – Programa Operacional Competitividade e Internacionalização by these grants: UID/FIS/04434/2019; UIDB/04434/2020; UIDP/04434/2020; PTDC/FIS-AST/32113/2017 & POCI-01-0145-FEDER-032113; PTDC/FIS-AST/28953/2017 & POCI-01-0145-FEDER-028953. V.A. acknowledges the support from FCT through Investigador FCT contract nr. IF/00650/2015/CP1273/CT0001. N.J.N. acknowledges support form the following projects: UIDB/04434/2020 & UIDP/04434/2020, CERN/FIS-PAR/0037/2019, PTDC/FIS-OUT/29048/2017, COMPETE2020: POCI-01-0145-FEDER-028987 & FCT: PTDC/FIS-AST/28987/2017. The INAF authors acknowledge financial support of the Italian Ministry of Education, University, and Research with PRIN 201278X4FL and the "Progetti Premiali" funding scheme. JLB acknowledges financial support from "la Caixa" Foundation (ID 100010434) under the fellowship LCF/BQ/PI20/11760023, and from the European Union's Horizon 2020 research and innovation programme under the Marie Skłodowska-Curie grant agreement No 847648. AW acknowledges the financial support of the SNSF by grant number P400P2_186765. SGS acknowledges the support from FCT through Investigador FCT contract nr. CEECIND/00826/2018 and POPH/FSE (EC). ODSD is supported in the form of a work contract (DL 57/2016/CP1364/CT0004) funded by FCT. We would like to thank the anonymous referee for their thorough and thoughtful comments that greatly improved the quality of the manuscript.

References

Agúndez, M., Parmentier, V., Venot, O., Hersant, F., & Selsis, F. 2014, A&A, 564, A73
Allart, R., Lovis, C., Pino, L., et al. 2017, A&A, 606, A144
Allart, R., Pino, L., Lovis, C., et al. 2020, A&A, 644, A155
Arcangeli, J., Désert, J.-M., Line, M. R., et al. 2018, ApJ, 855, L30
Barstow, J. K. 2020, MNRAS, 497, 4183
Baxter, C., Désert, J.-M., Parmentier, V., et al. 2020, A&A, 639, A36
Bohn, A. J., Southworth, J., Ginski, C., et al. 2020, A&A, 635, A73
Borsa, F., Allart, R., Casasayas-Barris, N., et al. 2021, A&A, 645, A24
Bourrier, V., Kitzmann, D., Kuntzer, T., et al. 2020, A&A, 637, A36
Brogi, M., & Line, M. R. 2019, AJ, 157, 114
Brogi, M., de Kok, R. J., Albrecht, S., et al. 2016, ApJ, 817, 106
Casasayas-Barris, N., Pallé, E., Yan, F., et al. 2019, A&A, 628, A9
Casasayas-Barris, N., Palle, E., Stangret, M., et al. 2021, A&A, 647, A26
Cauley, P. W., Shkolnik, E. L., Llama, J., & Lanza, A. F. 2019, Nat. Astron., 3, 408
Cauley, P. W., Wang, J., Shkolnik, E. L., et al. 2021, AJ, 161, 152
Ehrenreich, D., Tinetti, G., Lecavelier Des Etangs, A., Vidal-Madjar, A., & Selsis, F. 2006, A&A, 448, 379
Ehrenreich, D., Lovis, C., Allart, R., et al. 2020, Nature, 580, 597
Evans, T. M., Sing, D. K., Kataria, T., et al. 2017, Nature, 548, 58
Evans, T. M., Sing, D. K., Goyal, J. M., et al. 2018, AJ, 156, 283
Fisher, C., & Heng, K. 2019, ApJ, 881, 25
Fortney, J. J., Lodders, K., Marley, M. S., & Freedman, R. S. 2008, ApJ, 678, 1419
Gandhi, S., & Madhusudhan, N. 2019, MNRAS, 485, 5817
Gandhi, S., Madhusudhan, N., & Mandell, A. 2020, AJ, 159, 232
Gao, P., Thorngren, D. P., Lee, G. K. H., et al. 2020, Nat. Astron., 4, 951
Gebek, A., & Oza, A. V. 2020, MNRAS, 497, 5271
Gibson, N. P., Merritt, S., Nugroho, S. K., et al. 2020, MNRAS, 493, 2215
Haynes, K., Mandell, A. M., Madhusudhan, N., Deming, D., & Knutson, H. 2015, ApJ, 806, 146
Heng, K., Wyttenbach, A., Lavie, B., et al. 2015, ApJ, 803, L9
Herman, M. K., de Mooij, E. J. W., Jayawardhana, R., & Brogi, M. 2020, AJ, 160, 93
Hoeijmakers, H. J., Ehrenreich, D., Kitzmann, D., et al. 2019, A&A, 627, A165
Hoeijmakers, H. J., Seidel, J. V., Pino, L., et al. 2020, A&A, 641, A123
Huang, C., Arras, P., Christie, D., & Li, Z.-Y. 2017, AAS Meeting Abs., 229, 301.01
Hubeny, I., Burrows, A., & Sudarsky, D. 2003, ApJ, 594, 1011
Kausch, W., Noll, S., Smette, A., et al. 2015, A&A, 576, A78
Keles, E., Kitzmann, D., Mallonn, M., et al. 2020, MNRAS, 498, 1023
Kesseli, A. Y., & Snellen, I. A. G. 2021, ApJ, 908, L17
Knutson, H. A., Charbonneau, D., Allen, L. E., Burrows, A., & Megeath, S. T. 2008, ApJ, 673, 526
Kreidberg, L., Line, M. R., Parmentier, V., et al. 2018, AJ, 156, 17
Lavie, B., Mendonça, J. M., Mordasini, C., et al. 2017, AJ, 154, 91
Lecavelier Des Etangs, A., Pont, F., Vidal-Madjar, A., & Sing, D. 2008, A&A, 481, L83
Line, M. R., Fortney, J. J., Marley, M. S., & Sorahana, S. 2014, ApJ, 793, 33
Line, M. R., Stevenson, K. B., Bean, J., Kreidberg, L., & Fortney, J. J. 2016, AAS Meeting Abs., 227, 224.03
Liu, J., & Schneider, T. 2010, J. Atm. Sci., 67, 3652
Lodders, K. 2003, ApJ, 591, 1220
Lothringer, J. D., & Barman, T. 2019, ApJ, 876, 69
Louden, T., & Wheatley, P. J. 2015, ApJ, 814, L24
Mollière, P., van Boekel, R., Dullemond, C., Henning, T., & Mordasini, C. 2015, ApJ, 813, 47
Nugroho, S. K., Kawahara, H., Masuda, K., et al. 2017, AJ, 154, 221
Nugroho, S. K., Gibson, N. P., de Mooij, E. J. W., et al. 2020, ApJ, 898, L31
Parmentier, V., Line, M. R., Bean, J. L., et al. 2018, A&A, 617, A110
Parmentier, V., Showman, A. P., & Fortney, J. J. 2021, MNRAS, 501, 78
Pepe, F., Cristiani, S., Rebolo, R., et al. 2021, A&A, 645, A96
Pino, L., Ehrenreich, D., Wyttenbach, A., et al. 2018, A&A, 612, A53
Pino, L., Désert, J.-M., Brogi, M., et al. 2020, ApJ, 894, L27
Powell, D., Louden, T., Kreidberg, L., et al. 2019, ApJ, 887, 170
Ridden-Harper, A. R., Snellen, I. A. G., Keller, C. U., et al. 2016, A&A, 593, A129
Salz, M., Schneider, P. C., Czesla, S., & Schmitt, J. H. M. M. 2016, A&A, 585, L2
Seidel, J. V., Ehrenreich, D., Wyttenbach, A., et al. 2019, A&A, 623, A166
Seidel, J. V., Ehrenreich, D., Bourrier, V., et al. 2020a, A&A, 641, L7
Seidel, J. V., Ehrenreich, D., Pino, L., et al. 2020b, A&A, 633, A86
Seidel, J. V., Lendl, M., Bourrier, V., et al. 2020c, A&A, 643, A45
Serindag, D. B., Nugroho, S. K., Mollière, P., et al. 2021, A&A, 645, A90
Sheppard, K. B., Mandell, A. M., Tamburo, P., et al. 2017, ApJ, 850, L32
Showman, A. P., Fortney, J. J., Lian, Y., et al. 2009, ApJ, 699, 564
Showman, A. P., Tan, X., & Zhang, X. 2018, in AGU Fall Meeting Abstracts, 2018, P43E–3818
Skilling, J. 2006, Bayesian Anal., 1, 833
Smette, A., Sana, H., Noll, S., et al. 2015, A&A, 576, A77
Snellen, I. A. G., de Kok, R. J., de Mooij, E. J. W., & Albrecht, S. 2010, Nature, 465, 1049
Snellen, I. A. G., Brandl, B. R., de Kok, R. J., et al. 2014, Nature, 509, 63
Southworth, J., Bohn, A. J., Kenworthy, M. A., Ginski, C., & Mancini, L. 2020, A&A, 635, A74
Steinrueck, M. E., Parmentier, V., Showman, A. P., Lothringer, J. D., & Lupu, R. E. 2019, ApJ, 880, 14
Stock, J. W., Kitzmann, D., Patzer, A. B. C., & Sedlmayr, E. 2018, MNRAS, 479, 865
Tabernero, H. M., Zapatero Osorio, M. R., Allart, R., et al. 2021, A&A, 646, A158
Trotta, R. 2008, Contemp. Phys., 49, 71
West, R. G., Hellier, C., Almenara, J. M., et al. 2016, A&A, 585, A126
Wyttenbach, A., Ehrenreich, D., Lovis, C., Udry, S., & Pepe, F. 2015, A&A, 577, A62
Wyttenbach, A., Lovis, C., Ehrenreich, D., et al. 2017, A&A, 602, A36
Wyttenbach, A., Mollière, P., Ehrenreich, D., et al. 2020, A&A, 638, A87
Yan, F., Espinoza, N., Molaverdikhani, K., et al. 2020, A&A, 642, A98
Zhang, X. 2020, Res. Astron. Astrophys., 20, 099

Appendix A: Posterior distributions of the retrievals

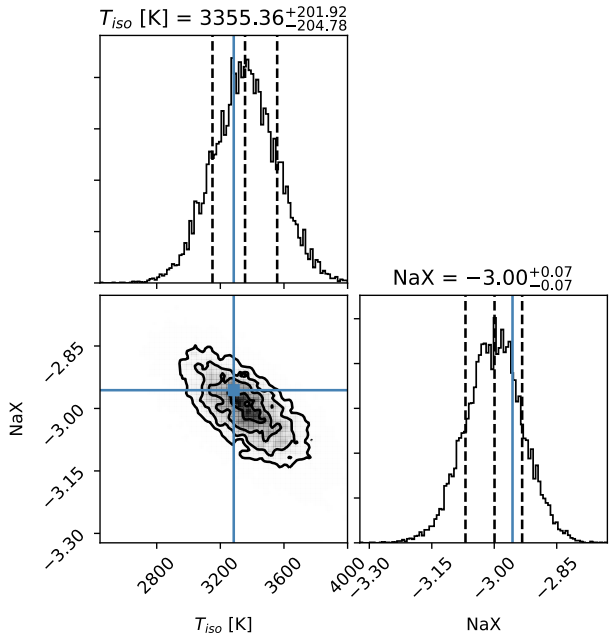

Fig. A.1. Posterior distribution of isothermal line retrieval. This was used as the base model to which all other scenarios were compared.

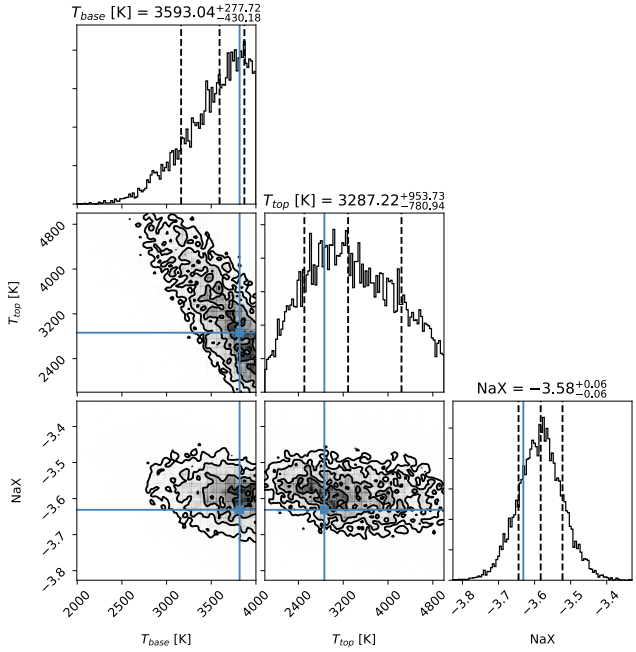

Fig. A.2. Posterior distribution of temperature gradient line retrieval. $T_{\rm base}$ is at the surface of the planet, and $T_{\rm top}$ at the top of the probed atmosphere.

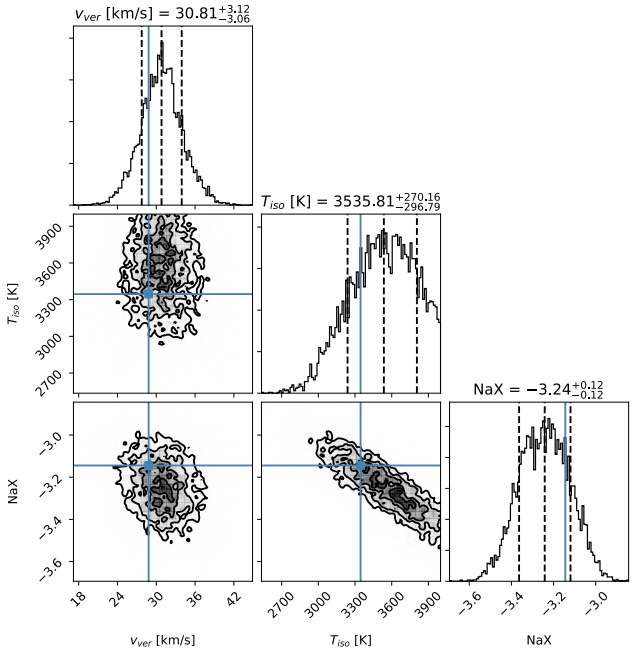

Fig. A.3. Posterior distribution of isothermal line retrieval with an added vertical wind constant throughout the atmosphere.

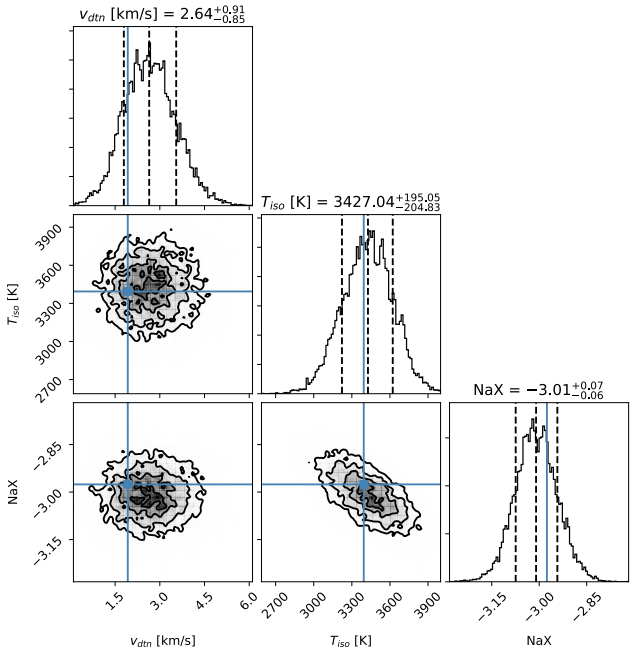

Fig. A.4. Posterior distribution of isothermal line retrieval with an added constant day- to nightside wind throughout the atmosphere.

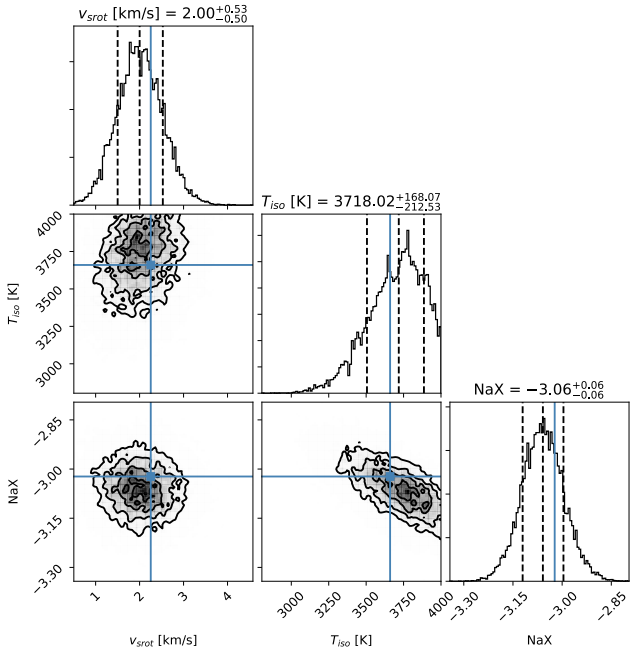

Fig. A.5. Posterior distribution of isothermal line retrieval with an added constant super-rotational wind throughout the atmosphere.

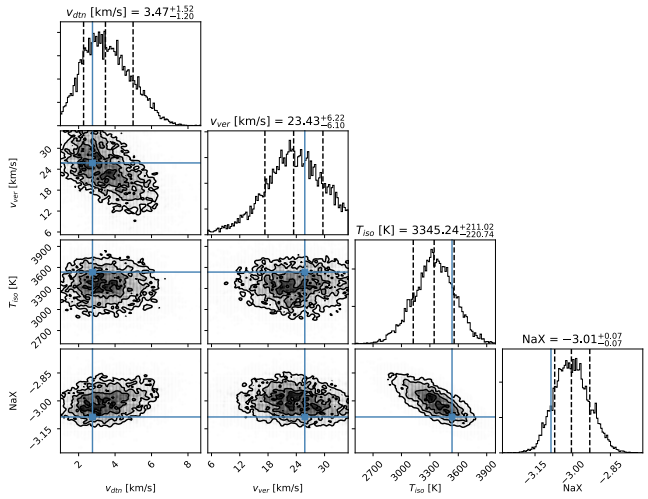

Fig. A.6. Posterior distribution of isothermal line retrieval with an added day- to nightside wind in the lower atmosphere and a vertical wind in the upper atmosphere. The change in the layers was set at $p = 10^{-4}$ bar, with the surface pressure at $P_0 = 10$ bar.

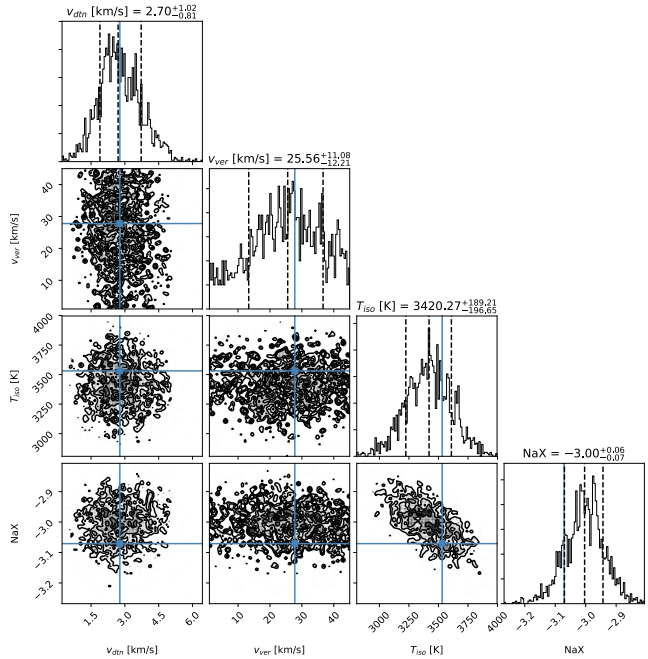

Fig. A.7. Posterior distribution of isothermal line retrieval with an added day- to nightside wind in the lower atmosphere and a vertical wind in the upper atmosphere. The change in the layers was set at $p = 10^{-5}$ bar, with the surface pressure at $P_0 = 10$ bar.

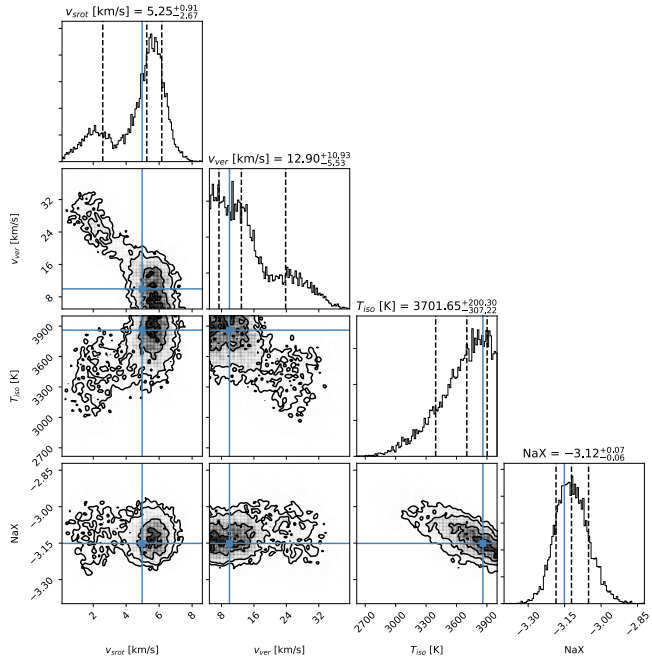

Fig. A.8. Posterior distribution of isothermal line retrieval with an added super-rotational side wind in the lower atmosphere and a vertical wind in the upper atmosphere. The change in the layers was set at $p = 10^{-3}$ bar, with the surface pressure at $P_0 = 10$ bar.

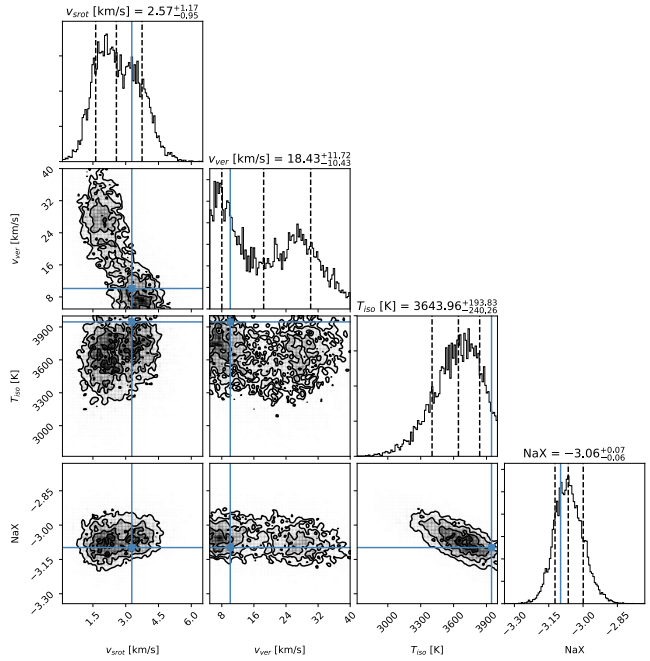

Fig. A.9. Posterior distribution of isothermal line retrieval with an added super-rotational side wind in the lower atmosphere and a vertical wind in the upper atmosphere. The change in the layers was set at $p = 10^{-4}$ bar, with the surface pressure at $P_0 = 10$ bar.

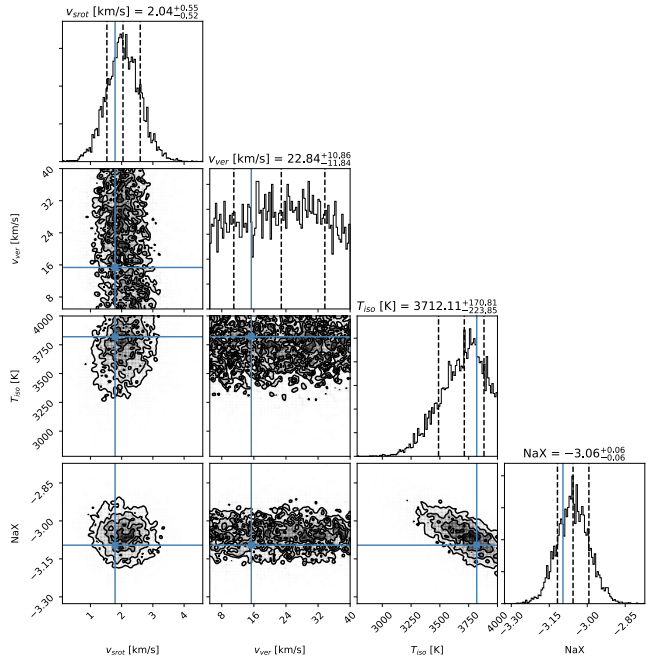

Fig. A.10. Posterior distribution of isothermal line retrieval with an added super-rotational side wind in the lower atmosphere and a vertical wind in the upper atmosphere. The change in the layers was set at $p = 10^{-5}$ bar, with the surface pressure at $P_0 = 10$ bar.

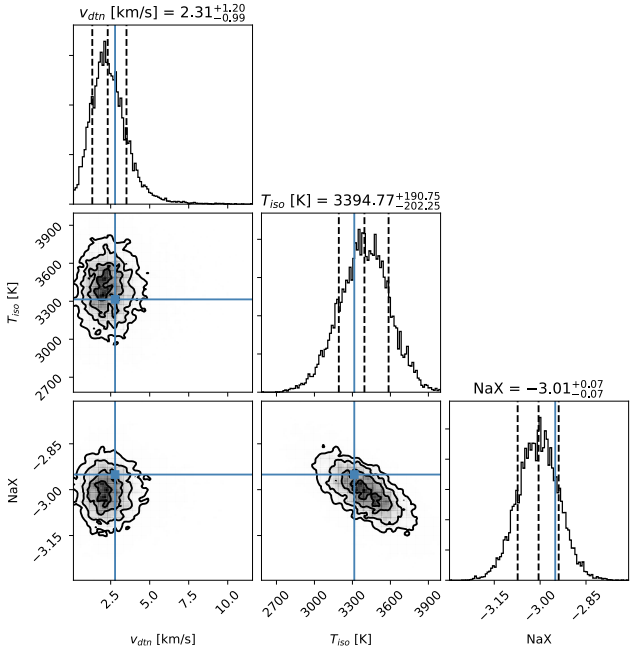

Fig. A.11. Posterior distribution of isothermal line retrieval with an added day- to nightside wind dependent on the latitude through $\cos\theta$.

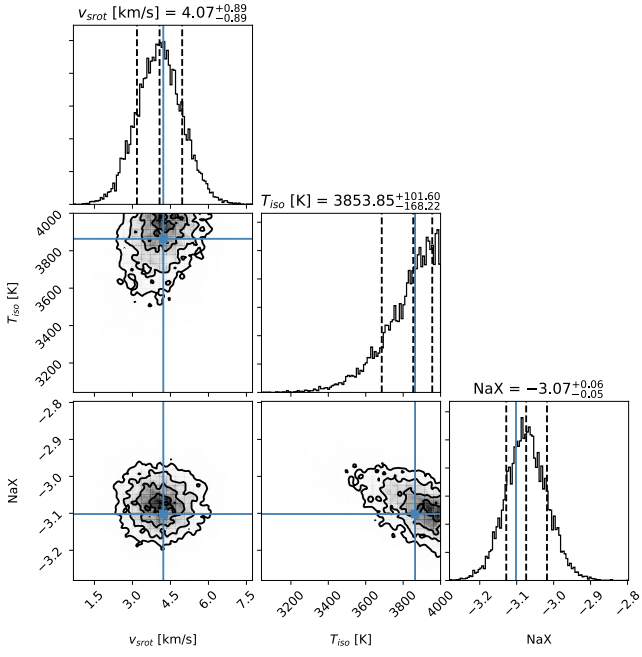

Fig. A.12. Posterior distribution of isothermal line retrieval with an added super-rotational wind dependent on the latitude through $\cos\theta$.

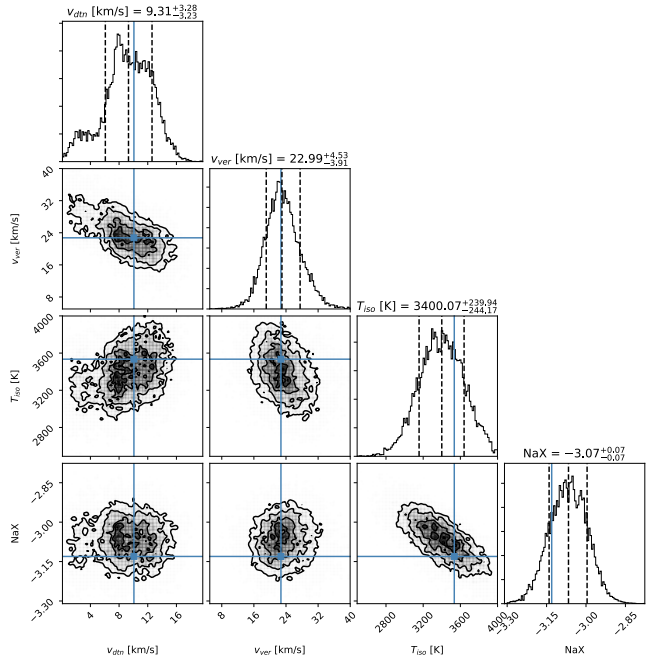

Fig. A.13. Posterior distribution of isothermal line retrieval with an added $\cos\theta$ dependent day- to nightside wind in the lower atmosphere and a vertical wind in the upper atmosphere. The change in the layers was set at $p = 10^{-3}$ bar, with the surface pressure at $P_0 = 10$ bar.

Appendix B: Discussion of the planetary orbital velocity

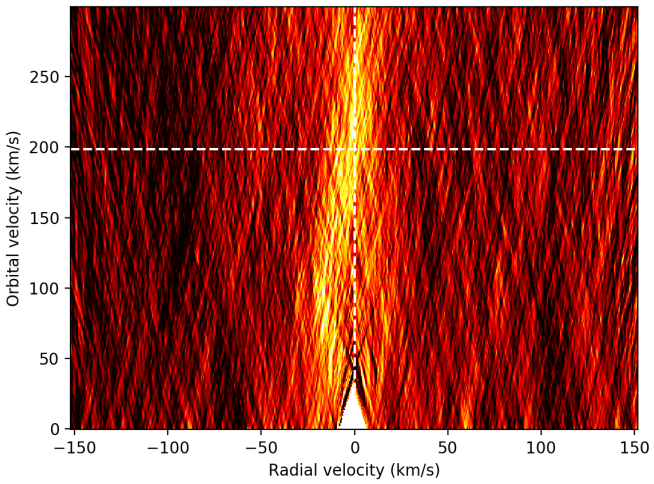

Fig. B.1. K_p-v_{sys} map generated from the two ESPRESSO nights, the position of the sodium line as calculated in Ehrenreich et al. (2020) is indicated as dashed white lines. White areas stem from the masking of the data at the centre of the stellar sodium lines. Lighter colours indicate a stronger detection signal.

To strengthen our argument that the line shape indeed stems from the dynamical structure of the exoplanet atmosphere and not from factors related to the orbital motion, we studied the effect of the planetary orbital motion (K_p) and its uncertainty on our results. In our analysis, we used the value of K_p as calculated from the stellar mass, period, and inclination by Ehrenreich et al. (2020).

However, to demonstrate the effect of K_p on the sodium doublet line shape, we also derived K_p directly from the signal of the planetary sodium (see Figure B.1). Figure B.1 shows the K_p - v_{sys} space, where we combined the ESPRESSO transits and the two sodium lines to generate the signal. We excluded the HARPS data from this demonstration to keep re-binning at a minimum and the signal shape as precise as possible.

The map presented in Figure B.1 confirms the sodium signal that was already independently established with the HARPS spectrograph (Seidel et al. 2019) and the ESPRESSO spectrograph (Tabernero et al. 2021), and it also confirms its broad line shape. However, the map also demonstrates the difficulties encountered when K_p is directly derived from the data of single lines instead of hundreds or even thousands of spectral lines (see e.g. Hoeijmakers et al. 2020). The signal is too broad in K_p to properly derive a precise value, spanning from roughly 50 to 250 km s^{-1} due to the low number of available lines.

It also demonstrates that the line shape is independent of small errors on K_p because we sampled very similarly broad profiles for values of K_p varying up to 10 km s^{-1} from the value derived in Ehrenreich et al. (2020). The value of K_p as calculated by Ehrenreich et al. (2020) therefore is preferred to our own calculation for two reasons: it is much more precise with a value of 196.52 ± 0.94 km s^{-1}, which translates into a maximum error at ingress and egress of ±0.3 km s^{-1} (less than one ESPRESSO pixel). Additionally, in their calculation, they do not take the in-transit data into account and decoupled the calculation of K_p from any atmospheric dynamics. This makes any retrieval of the atmospheric dynamics more robust against the effect of orbital motion.

In conclusion, the derivation of K_p from our dataset has shown that the sodium signal exists and that its line shape can only be explained by broadening winds or other atmospheric dynamics. The effect of the orbital motion on our results is negligible.